Numerical Investigation of Flexible Airfoil Aerodynamics

Sakhr Abu Darag, Yasser Nogoud, Musab Mohammed
Aeronautical Engineering Dept., Sudan University of Science and Technology (SUST), Sudan
sakhr.abudarag@sustech.edu

Received:24/04/2020
Accepted: 29/06/2020

ABSTRACT- A commercial CFD solver is used to simulate the unsteady aerodynamics performance of rigid and flexible wing airfoils for a high-performance jet trainer aircraft. The configuration used in the computational analysis is NACA 64012. In the numerical simulations the turbulence is modeled by enhancing Spalart-Allmaras turbulence model. To simulate the fluttering motion of the upper surface, an algorithm written in C computer language is integrated with the Fluent. The program controls the oscillation of the upper suction surface to specific defined displacement and the mesh dynamic that adjacent to the moving surface of the airfoil. The numerical experiments for both, rigid and flexible airfoils are carried out at flight speed of 85 m/s and angle of attack from zero to 18 degree. In order to verify the results of numerical simulation, the solver is validated against prior experiment of a lift coefficient. In comparison between rigid and flexible airfoils, the aerodynamic forces produced by a flexible airfoil shows that the lift coefficient is increased by 10% for angle of attack ranging from the incidence degree to 10 degree and then decreased slightly till the stall angle located at 16 degree. The flow separation in rigid airfoil is predicted at 7.5% of airfoil chord, whereas in the flexible airfoil it is at 59% of the airfoil chord.

Keywords*: Flexible airfoil, turbulent flow, fluttering motion, lift coefficient, flow separation.*

المستخلص– تم استخدام CFD لمحاكاة أداء الديناميكا الهوائية الغير مستقر لجنيح صلب ومرن لطائرة تدريب نفاثة عالية الأداء. النموذج الذي تم إستخدامه في التحليل الحسابي هو NACA 64012. عند إجراء المحاكاة، تم نمذجة الاضطراب الهوائي عن طريق موديل Spalart-Allmaras. لمحاكاة حركة الرفرفة للسطح العلوي، تم إضافة خوارزمية مكتوبة بلغة الكمبيوتر C إلي برنامج Fluent. يتحكم المحاكي في اهتزاز السطح العلوي للجنيح لإزاحة محددة وكذلك ديناميكية الشبكة المجاورة للسطح المتحرك للجنيح. تم إجراء التجارب الحاسوبية لكل من الجنيح الصلب والمرن عند سرعة طيران 85 م/ث وزاوية هجوم تتدرج من الصفر إلى 18 درجة. من أجل التحقق من نتائج المحاكي، تمت مقارنة النتائج مع تجربة معملية سابقة لتحديد معامل الرفع. عند المقارنة بين الجنيح الصلب والمرن، أظهرت القوى الديناميكية الهوائية الناتجة عن الجنيح المرن أن معامل الرفع يزداد بنسبة 10% لزاوية هجوم تتراوح من درجة الصفر إلى 10 درجات ثم ينخفض تدريجياً حتى زاوية أنفصال الهواء عند 16 درجة. تم التأكيد على إنفصال الهواء في الجنيح الصلب عند 7.5% من وتر الجنيح بينما في الجنيح المرن يحدث الإنفصال عند 59% من وتر الجنيح.

Introduction

Wings are the essential part of the aircraft structure. They serve to produce major part of the lift and they also maintain lateral stability and provide space of fuel storage. In most airplanes the undercarriage and the engines are fixed in the wing. In conventional aircraft utilizing a rigid wing, the shape of the wing is optimized corresponding to the control surfaces system such as ailerons, flaps and rudder, while in the modern airplane enhancing a flexible wing, in addition to the control surfaces, the shape of the wing is changed by elastic deflection movement of some parts of the wing structure corresponding to the phase of flight that required [1].

The flexible wing is defined as a wing that fabricated by smart materials with actuators able to change its shape depending on the situation in order to optimize aerodynamic performance and aircraft control. David Munday et al. were conducted experimental exercises for a flexible wing model [2]. One of these tasks was considered a comparison between flexible wing model and conventional wing model in wind tunnel at Re =

2.5×10^4 and angle of attack ranging from zero to 9 degrees to illustrate the effects of fluttering on flow separation. They used actuators attached to the flexible surface to govern the fluttering motion of the upper surface of the wing.

Their results represented a clear delay in flow separation reached to 10% of chord at angle of attack 9 degrees when the flexible wing model was used instead of the conventional wing model. Since the critical factor for the Micro Aerial Vehicle MAV flight is the coupling of aerodynamics and structural dynamics, Satish K. Chimakurthi et al. [3] represented a computational framework for simulating shell-like flexible wing structures flapping in incompressible flow at low Reynolds numbers in both hover and forward flight. They were developed a framework coupling an in-house Co-rotational finite element Structural Dynamics solver CSD to an in-house pressure-based Navier-Stokes solver.

The results were validated versus experimental data and developed aeroelasticity codes for both the CSD and the aeroelastic solvers enhancing different wing configurations. A research group from University of Maryland also simulated the aerodynamics characteristics of flexible flapping wings for MAV applications [4]. They implemented a coupled CFD-CSD solver. For CFD analysis, the solver in-house compressible RANS solver was used whereas for investigation of structural dynamics, the dynamics solver MBDyn was utilized after some modification.

The results for the coupled codes were validated against available experimental results to predict the expected profile for a spanwise flexible wing in pure plunge. An integrated study of flexible wing aerodynamics of flapping MAV was also preceded by enhancing an in-house computational fluid dynamic solver combined with experimental data [5]. The researchers built a realistic wing planform CFD model with a capability to mimic realistic flexible wing kinematics in order to predict an unsteady aerodynamics of four-winged MAV.

The main purpose of the present paper is to improve the aerodynamic characteristics of the wing by implementing fluttering motion to upper surface of the wing. The fluttering motion is simulated by integrating specific code that represents the motion to the commercial software package (Fluent).

Computational Analysis

The airfoil NACA 64012 is used as a model drawn in AutoCAD software program. The maximum thickness of the airfoil is correlated to the fluttering motion of the upper surface according to certain limitations such as surface length and arc radius. Therefore, to optimize satisfactory aerodynamics characteristics, the effect of the flexible surface length should be studied.

The effect of the flexible surface length on the aerodynamics characteristics of the airfoil is examined by testing two surfaces with different lengths. Figure 1 shows the airfoil geometry of NACA 64012 with two different lengths of flexible surfaces used for the simulation. One of them with chordwise length of 0.69 m started at point 0.05m behind the leading edge and the second flexible airfoil with length of 0.76 m started at point 0.03 m behind the leading edge.

The different started points of these flexible surfaces is governed by the leading edge radius and the length of the trailing edge control surface such as ailerons or lift devices (flaps). The origin of arc radius is located at maximum thickness of the airfoil which considered as vertical reference. The results reveal that, the longest surface is perform better aerodynamics properties than the shorter one, therefore it's considered for this study.

The flight conditions for both, the rigid and flexible airfoils are explained in Table 1.

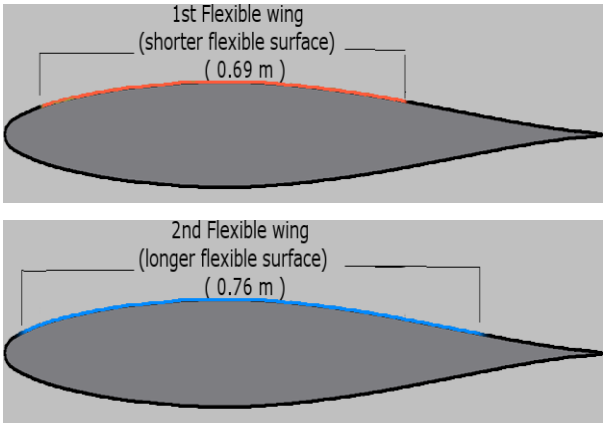

Figure 1: The two different lengths of the flexible surfaces

Grid Generation

The structured grid is generated using Gambit software. Then it is replaced by unstructured grid due to presence of negative volumes during the running of the dynamic mesh motion.

TABLE 1: FLIGHT CONDITIONS

Item	*Description*
Altitude	At sea level
Temperature	288 K
Flight speed	0.25 Mach (85 m/s)
Air Density	1.225 kg/m^3
Air static pressure	101.325 KPa
Reynolds Number	5.8.10^6

Therefore, the boundary layer meshing option in Gambit is not applied to the present study in order to avoid negative volumes. Instead of using the structured mesh and boundary layer, the boundary adaption technique around the airfoil is implemented in order to allow for convenient mapping of the internal grid points on the dynamic flexible surface by increasing the number of nodes as illustrated in Figure 2.

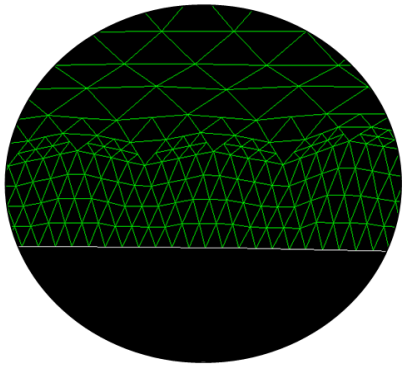

(a)

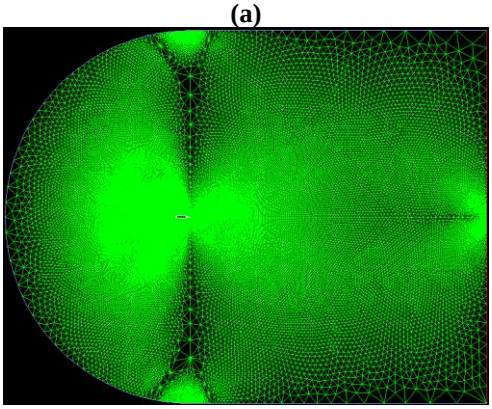

(b)

Figure 2: Unstructured mesh after the adaption (a) Upper surface of the airfoil (b) The whole domain (c-mesh)

The boundary adaptation technique has been investigated extensively by many authors among them Liseikin [6]. The technique act to split the mesh cells into more cells, therefore more accuracy is gained. Generally, they are divided into differential and algebraic techniques. Differential technique is based on the solution of the Euler-Lagrange Differential Equations, often solved simultaneously with other fluid flow equations when the mesh is adapted. Algebraic technique is based on a direct equidistribution process which does not require solution of the Differential Equations and therefore, it requires less computational effort. The number of nodes and cells around the airfoil is increased by 11089 after adaption to become 76021 nodes and cells.

Boundary Conditions

Boundary conditions determination for the present case study is based on the domain of test section which is classified into three parts, two of them are defined as airflow inlet zones named as farfield 1 and farfield 2 and the third part is an outlet flow zone named farfield 3 as illustrated in Figure 3. The airfoil consists of three parts, upper surface, lower surface and flexible surface. This division represented in Figure 4 enables to apply the dynamic mesh motion of the flexible surface.

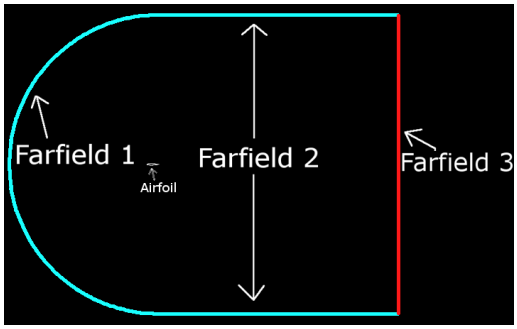

Figure 3: Flow Domain

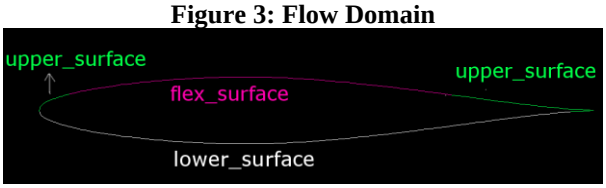

Figure 4: Airfoil Definition

The boundary conditions are specified for the zones as shown in Table 2. Define the velocity vector at the inlet flow as a boundary condition requires to determine the velocity components u and v in Cartesian Coordinates from the flight speed and angle of attack.

Governing equations of incompressible flow

The governing equations of incompressible flow in Cartesian coordinates [7] are:

Mass conservation equation:

$$1)\left(\frac{\partial u_i}{\partial x_i} = 0\right.$$

where, u is the velocity. Momentum equation:

$$(2)\quad \frac{\partial u_i}{\partial t} + u_j \frac{\partial u_i}{\partial x_j} = -\frac{\partial p}{\partial x_i} + \mu\left(\frac{\partial^2 u_i}{\partial u_j^2}\right)$$

where, t is time, p is the pressure, μ is dynamic viscosity and *i=1,2,3 for x,y,z* coordinates

TABLE 2: BOUNDARY CONDITIONS ZONES

BC	Zone	BC Definition
Inflow	Farfield 1	Velocity-inlet
	Farfield 2	Velocity-inlet
Outflow	Farfield 3	Pressure-outlet
Airfoil	Flex surface	Wall
	Upper surface	Wall
	Lower surface	Wall

Turbulence modeling

The Spalart-Allmaras turbulence model that solves a modeled transport equation for the kinematic eddy (turbulent) viscosity is used to model the turbulence. The model was designed for aerospace applications involving wall-bounded flows and has represented satisfactory results for boundary layers subjected to adverse pressure gradients [8].

This one equation model is derived using empiricism and arguments of dimensional analysis, Galilean invariance, and selective dependence on the molecular viscosity [9]. The model solves a partial differential equation (3), over the entire field for $\tilde{v}$, from which the turbulent kinetic viscosity v_t can be extracted.

$$\frac{\partial \tilde{v}}{\partial t} + u_j \frac{\partial \tilde{v}}{\partial x_j} = C_{b1}[1 - f_{t2}]\tilde{S}\,\tilde{v} + \frac{1}{\sigma}\{\nabla \cdot [(v + \tilde{v})\nabla\tilde{v}] + C_{b2}|\nabla\tilde{v}|^2\}$$

$$-\left[C_{\omega 1} f_\omega - \frac{C_{b1}}{\kappa^2} f_{t2}\right]\left(\frac{\tilde{v}}{d}\right)^2 + f_{t1}\Delta U^2 \quad (3)$$

$$\tilde{S} \equiv S + \frac{\tilde{v}}{\kappa^2 d^2} f_{v1}\ , f_{v2} = 1 - \frac{x}{1 + x f_{v1}}$$

where,

$$S = \sqrt{2\Omega_{ij}\Omega_{ij}}$$

$$\Omega_{ij} \equiv \frac{1}{2}\left(\frac{\partial u_i}{\partial x_j} - \frac{\partial u_j}{\partial x_i}\right)$$

$$f_\omega = g\left[\frac{1 + C_{\omega 3}^6}{g^6 + C_{\omega 3}^6}\right]^{1/6}, g = r + C_{\omega 2}(r^6 - r) \quad ,$$

$$r \equiv \frac{\tilde{v}}{\tilde{S}\kappa^2 d^2}$$

$$f_{t1} = C_{t1} g_t exp\left(-C_{t2}\frac{\omega_t^2}{\Delta U^2}[d^2 + g_t^2 d_t^2]\right)$$

$$f_{t2} = C_{t3} exp(-C_{t4} x^2)$$

d is the distance to the closest surface

The constants are

$\sigma = 2/3$,$C_{b1} = 0.1355$, $C_{b2} = 0.622$, $\kappa = 0.41$, $C_{\omega 1} = \frac{C_{b1}}{\kappa^2} + \frac{1 + C_{b2}}{\sigma}$

$C_{\omega 2} = 0.3$,$C_{\omega 3} = 2$,$C_{v1} = 7.1$,$C_{t1} = 1$,$C_{t2} = 2$,$C_{t3} = 1.1$,$C_{t4} = 2$

On the walls the "no-slip condition" is considered, therefore the dependent variable $\tilde{v}$ is set to zero. For tangent-flow surfaces, a zero-pressure gradient is applied. Farfield boundary condition as shown in table 2 is applied for outflow boundaries by extrapolating $\tilde{v}$ from the interior passing flow. The farfield boundary condition at the inflow is perused from the free stream. The eddy viscosity v_t is given by:

$$v_t = \tilde{v} f_{v1}$$

where the viscous damping function f_{v1} is integrated in order to properly reduce the turbulent viscosity in the viscous sub-layer. The damping function is given by:

$$f_{v1} = \frac{\chi^3}{\chi^3 + C_{v1}^3} \quad ; \quad X = \frac{\tilde{v}}{v}$$

The flexible surface preparation

The nature of motion required for flexible surface simulation is oscillatory motion that allows the arc radius of the upper surface of the airfoil to increase and decrease rapidly as illustrated in Figures 5 and 6. The oscillation range of the flexible upper surface is limited between the arc radius of the wing upper surface at normal airfoil profile condition and the maximum limit which governed by different factors such as the flexibility limitation of the wing structure and the flow aerodynamic characteristics. The oscillation motion of the flexible surface is defined as fluttering motion.

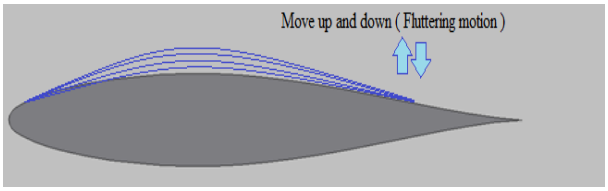

Figure 5: The manner of the flexible surface motion

The range of arc motion in y direction defines by *Y* as:

$$Y = -0.1 + 0.15 y_{full}\left(0.7(\sin\theta)^2 + 0.677\right) \quad (4)$$

$$y_{full} = y_{mag} - 0.1 \quad (5)$$

$$y_{mag} = \sqrt{R^2 - X^2} + 0.03 \quad (6)$$

where ymag specifies the length in x direction of the flexible surface and yfull is the actual displacement of the arc in y direction. R is the radius of the arc (maximum displacement of the thickness in meter).

The angle that dictates the motion of the arc, α:

$$\alpha = \omega t \quad (7)$$

where ω is the rotational speed. The angle that corresponds to the position of the original point, θ:

$$\theta = 2\alpha + \frac{3}{2}\pi \quad (8)$$

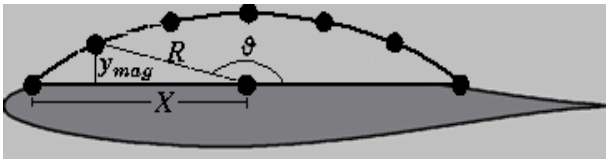

Figure 6: Fluttering motion of upper surface

The fluttering motion in commercial CFD program (Fluent) is performed by dynamic mesh option that permits the movement of the grid nodes. Therefore, all nodes that are adjacent to the upper surface of the airfoil are prepared to move in according to the motion of the flexible surface. To precede the process of flexible surface motion and it is limitations and the dynamic mesh, C program file has been established. The file contains the required data and equations that govern the motion of the flexible surface and adjacent grid nodes. Then the C-file is introduced to FLUENT solver by utilizing an intermediary program (Microsoft Visual Studio) that able to read and write C code file and illustrated it to FLUENT. Thereafter, the dynamic mesh setting is adjusted inside the FLUENT program. The procedure of adjustment of the dynamic mesh setting in FLUENT program is known as User-Defined Function Compiling (UDF). When the flexible surface moves, the adjacent grid nodes changed their distribution, which means the grid cells change their shapes according to the flexible surface motion as indicated in Figure 7. Different values for lift and drag coefficients are registered according to this phenomenon.

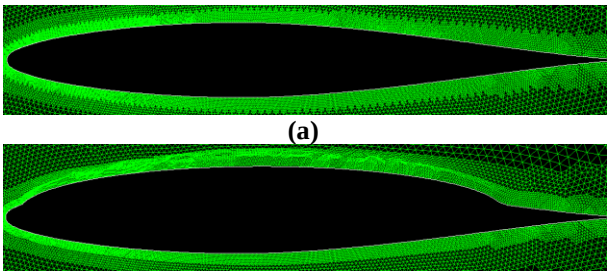

(a)

(b)

Figure 7: Grid around the airfoil (a) Before flexible surface motion (b) After flexible surface motion

Dynamic mesh setting has been adjusted in a specific method that ensures the proper motion of grid nodes and flexible surface. Before proceeding to dynamic mesh setup, it is significant to ensure that the software is solving for an unsteady state condition. The setup of the dynamic mesh in the commercial software solver is enhanced by applying four steps.

Firstly, the C code program file which contents the grid nodes motion and flexible surface motion specifications is integrated to the User-Defined Functions library (UDF) of FLUENT program. Secondly, the way of grid nodes motion is determined through the dynamic mesh parameter window. In this window, the grid nodes motion is determined as a ratio of cells splitting or collapsing which happened for the airfoil adjacent cells to the permissible range of the adjacent grid nodes, the expansion or contraction ratio of the cells and other properties.

In the third step, the movable surface and its movement manner are specified. These options are utilized in the software via dynamic mesh zones window. Lastly, run the test for specific time step size and number of time steps. The time step size used is 0.1 and 1st-Order implicit method of numerical discretization is adapted.

RESULTS AND DISCUSSIONS

The aerodynamic characteristics for both, rigid and flexible airfoils at flight speed of 0.25 Mach (85 m/s) and angles of attack ranging from zero to 18 degree are investigated. The velocity contours are displayed in Figure 8 for rigid airfoil at stall angle α=14°. The figure represents clearly the minimum velocity (zero assumption) in the stagnation point at the leading edge of the airfoil. Then the velocity increases gradually from leading edge to the rear of the airfoil. The wake behind the airfoil starts to propagate after the airfoil.

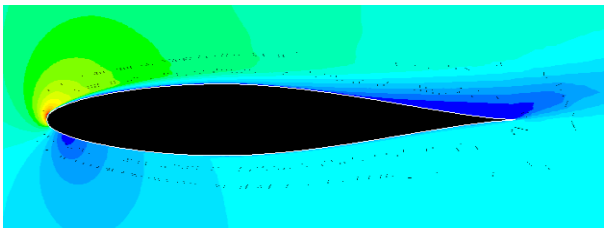

Figure 8: Velocity contour display of rigid airfoil

Moreover, the results for the velocity contour for flexible airfoil is plotted in Figure 9 at stall angle α=16°. The same scenario of velocity distribution is observed for flexible airfoil but with different velocity magnitudes spread over different chord lengths on the upper surface of the airfoil.

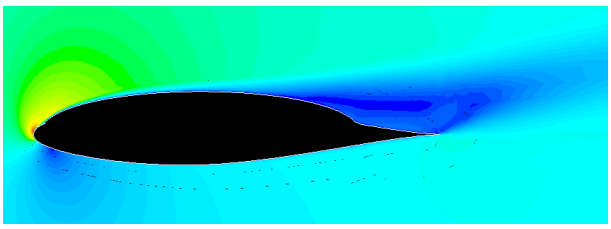

Figure 9: Velocity contour for flexible airfoil

Figures 10 and 11 indicate the lift and drag coefficients for both, rigid and flexible airfoils. For the rigid airfoil, the result of the lift coefficient indicates that the maximum lift coefficient $C_{L_{max}}$ is 1.3667 and the drag coefficient C_D is 0.039182 at stall angle of attack $\alpha_{STALL}=14^{o}$. Whereas for the flexible airfoil the maximum lift coefficient $C_{L_{max}}$ is 1.4048 and the drag coefficient C_D is 0.05998, both are occurred at stall angle of attack $\alpha_{STALL}=16^{o}$.

The lift coefficient of the flexible airfoil increases gradually with constant slope till angle of attack 10 degrees then continues in increasing with less slope till the maximum value 1.4048 at angle of attack 16 degrees. Whereas for the rigid airfoil it increases gradually with constant slope till the maximum lift coefficient $C_{L_{max}}$.

It is observed from the results that the lift coefficient for the flexible airfoil is increased by approximately 10% from the lift coefficient of the rigid wing till $C_l = 1.2$. Moreover, in Figure 10, when lift slope is zero, there is still a positive value of lift coefficient demonstrated for flexible airfoil condition. This property is similar to that induced by cambered airfoil at zero-lift line. The Figure also illustrates the maximum lift coefficient $C_{L_{max}}$ of flexible airfoil which is higher than its equivalent value in the rigid airfoil. In addition, the stall angle of attack α_{STALL} of the flexible airfoil is larger than the one in the rigid airfoil.

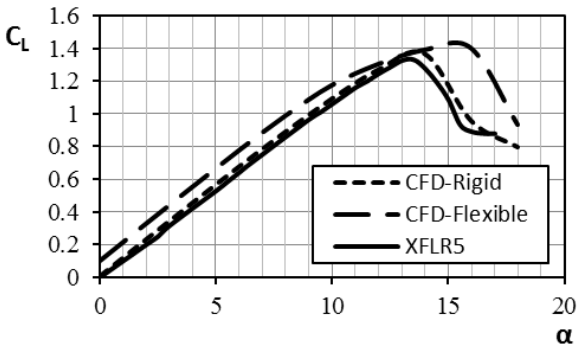

Figure 10: Lift coefficient vs angle of attack

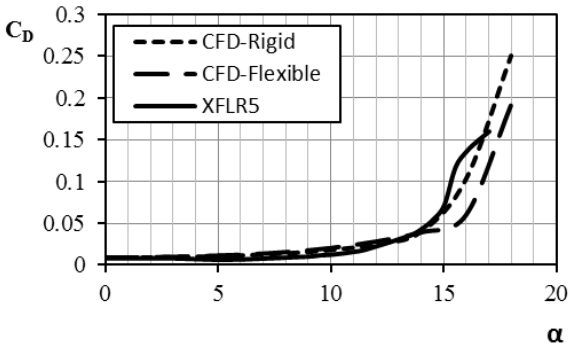

Figure 11: Drag coefficient vs angle of attack

To validate the investigation of rigid airfoil proceeded by computational programme FLUENT, the aerodynamic properties are plotted against the numerical XFLR5 [10] results. XFLR5 is software for the design of airfoils, wings and planes operating at low Reynolds numbers and using panel method or vortex lattice method. The same algorithms implemented in original XFoil code for foil analysis were used in XFLR5 tool.

In the latest version v4.00 of the code, a 3D panel method for wings and planes was introduced that enhancing modeling options for fuselages. For rigid airfoil the lift coefficient in both, XFLR5 and FLUENT results are in very close agreement in curve slope with only negligible slight variation through the stalling region. The linearity of the lift curve for XFLR5 is break down at 13.4 angle of attack whereas for FLUENT case the stall occurs beyond 14 degrees. Since the airfoil is symmetric, both lift curves go through the origin and then increase linearly with angle of attack till the maximum lift.

The cl_{max} calculated by XFLR5 is 1.3 and that predicted by FLUENT is found to be approximately equal to 1.4. In Figure 11 the drag coefficient of flexible airfoil is agreed very well with drag coefficient of rigid wing till the angle of attack 14 degrees where it starts to increase rapidly for rigid airfoil. The rapid increment in drag coefficient for flexible airfoil is delayed till angle of attack 16 degrees. From the results, it seems that the drag coefficient of the flexible airfoil is not affected by the increased thickness rather than separation starting onset.

Figure 11 also demonstrates the drag coefficient for rigid airfoil obtained by XFLR5 code in order to validate the computational analysis. The drag curve illustrated by XFLR5 results is completely corresponds with that by FLUENT analysis. The increasing of α_{STALL} value in flexible airfoil reveals in delay of the flow separation and damping of wake region for certain portion.

This result is clearly shown in Figures 12 and 13 where the velocity vectors are displayed for the flexible and rigid airfoils respectively at the angle of attack 16^{o}. The velocity vectors in these Figures were colored according to the velocity magnitude. The flow is separated in rigid airfoil at 0.075C.

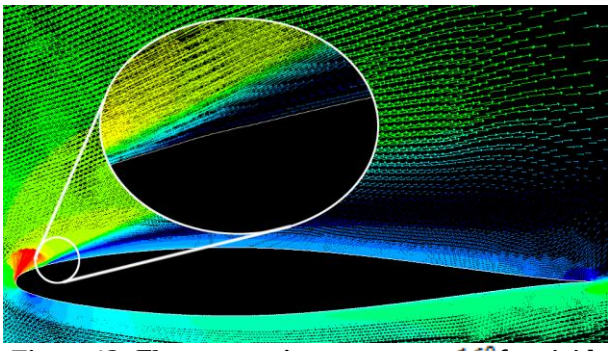

Figure 12: Flow separation onset at α =16^{o} for rigid airfoil

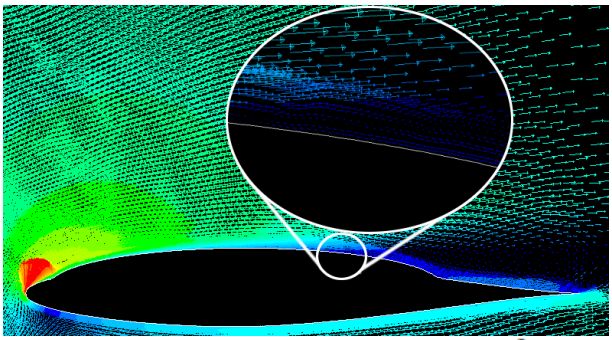

Figure 13: Flow separation onset at α =16^{o} for flexible airfoil

It means at (7.5% of airfoil chord), while in the flexible airfoil the separation is occurred at 0.59C (59% of airfoil chord), which illustrates clearly the delay of flow separation when the flexible airfoil is used. The delay of flow separation is caused by increasing the airfoil upper surface arc radius that leads to accelerate and energize the airflow over the upper surface.

Moreover, the increment in turbulent flow kinetic energy due to the oscillatory motion of the flexible surface may lead to damping both airflow circulation and wake region formation. The results for L/D ratio and polar curve are illustrated in Figures 14 and 15 respectively. The results of the flexible airfoil and rigid airfoil are plotted against a numerical XFLR5 result. Figure 14 indicates that the flexible airfoil has better L/D ratio than rigid airfoil at angles of attack ranging from zero to 6 degree, and at angles that higher than 14 degree. As a result, the flexible airfoil is more efficient in performing tasks at small vertical velocity.

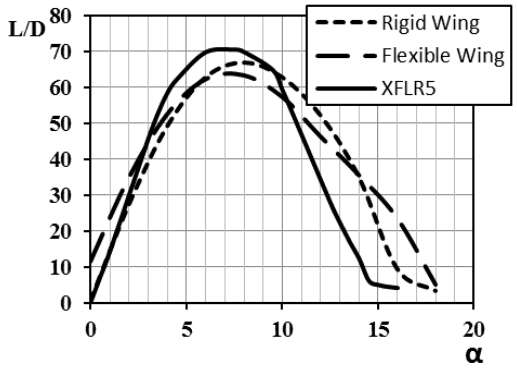

Figure 14: L/D ratio vs angle of attack α

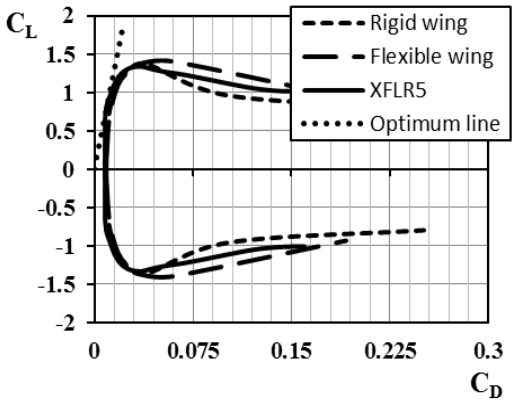

Figure 15: Polar curve

These velocities such as take-off run, steady flight, climb and descent and also at higher angles closed to stall angle of attack. The best efficiency point is

70 predicted at 7 degrees by XFLR5 code. The optimum point (minimum thrust required) as represented by Figure 15 is located at the intersection of tangent line with the polar curve. At this point the CLopt is 0.75 and the CDopt is 0.01. The parasite drag coefficient is almost coincided in the results of rigid and flexible airfoils. Whereas for induced drag of rigid airfoil, the lift coefficient obtained by CFD is more decreases with increase in drag coefficient than the lift coefficient of both, the flexible airfoil and the rigid airfoil that predicted by XFLR5.

CONCLUSION

The CFD investigation on the flexible and the rigid airfoils indicates that the flexible airfoil is capable to perform better aerodynamic results. In comparison between rigid and flexible airfoils, the aerodynamics forces produced by a flexible airfoil show that the lift coefficient is increased by 10% for angle of attack range till 10 degrees and then decreased slightly till the angle of stall 16 degrees while the stall angle of attack for the rigid airfoil is 14 degree. The flow separation in rigid airfoil is predicted at 7.5% of airfoil chord, whereas in the flexible airfoil is at 59% of the airfoil chord. L/D ratio confirms that the flexible airfoil performs more efficiently in most aircraft mission profile tasks beside the reduction in specific fuel consumption. Although the maximum lift coefficient of flexible airfoil is higher than the maximum lift coefficient of rigid airfoil, the lift optimum and the drag optimum are approximately the same for both. The total drag according to the results for rigid and flexible airfoils is function only on the induced drag, in other word on the lift coefficient. The parasite drag coefficient is satisfactory coincided for both, the rigid and flexible airfoils. The experimental investigation with flow visualization is highly recommended to validate the results. Extend the study of the prototype geometry from two dimensions to three dimensions is important to reduce the error between the experimental task and the real flight test result. In reality, there are many other factors influence the performance of wing must be considered such as the aero elasticity characteristics and vibration.

REFERENCES

[1] Takashi Atobe, (2008) "Pirior Studies for the Morphing-Wing in Fluid Dynamics Group" Fluid Dynamics Group - Japan aerospace Exploration Agency.

[2] David Munday, Jamey D. Jacoby, Thomas Hauser and George Huang, (2001) "Experimental and Numerical Investigation of Aerodynamic Flow Control Using Oscillating Adaptive Surfaces" AIAA 2001–2837.

[3] Satish K. Chimakurthi, Bret K. Stanford, Carlos E. S. Cesnik, and Wei Shyy, (2009) “Flapping Wing CFD/CSD Aeroelastic Formulation Based on a Corotational Shell Finite Element” 50th AIAA/ASME/ASCE/AHS/ASC Structures, Structural Dynamics, and Materials Conference, Palm Springs, California.

[4] Ria Malhan, James Baeder, Inderjit Chopra and Pierangelo Masarati, (2013) “CFD-CSD Coupled Aeroelastic Analysis of Flexible Flapping Wings for MAV Applications” University of Maryland, AIAA.

[5] Nakata T, Liu H, Tanaka Y, Nishihashi N, Wang X and Sato A., (2011) “Aerodynamics of a bio-inspired flexible flapping-wing micro air vehicle” Graduate School of Engineering, Chiba University, Chiba 263-8522, Japan.

[6] Liseikin V.D., (1998) “Algebraic Adaptation Based on Stretching Functions” Russian Journal for Numerical and Analytical Mathematical Modelling, Vol.13, No.4 307-324.

[7] David C. Wilcox, (2006) “Turbulence Modeling for CFD” Book, D C W Industries; 3rd edition (November 1, ISBN-13: 978-1928729082.

[8] John Anderson, (1995) “Computational Fluid Dynamics” Book, McGraw-Hill Education, 1 edition-ISBN-13: 978-0070016859.

[9] Spalart, P. R. and Allmaras, S. R., (1992) “A One-Equation Turbulence Model for Aerodynamic Flows” AIAA 92-0439, AIAA 30th Aerospace Science Meeting and Exhibit.

[10] Aerodyne, “Aerodynamics in Aero & Astro Engineering at Purdue”, Purdue University, https://engineering.purdue.edu/~aerodyn/ accessed on 13 Oct. 2020.